INVITED ARTICLE
doi: 10.2306/scienceasia1513-1874.2025.s011

*ScienceAsia* 51S (1): 2025: ID 2025s011: **1–11**

# 5, 6 - Dicyano [2, 1, 3] benzothiadiazole-based deep red/near-infrared thermally activated delayed fluorescence emitter for efficient electroluminescent devices

**Pattarapapa Janthakit**[a], **Jakkapan Kumsampao**[a], **Rattanasiri Wannapakdee**[a], **Atthapon Saenubol**[a], **Wijitra Waengdongbung**[a], **Taweesak Sudyoadsuk**[b], **Vinich Promarak**[a,*,†]

[a] Department of Materials Science and Engineering, School of Molecular Science and Engineering, Vidyasirimedhi Institute of Science and Technology, Rayong 21210 Thailand

[b] Frontier Research Center, Vidyasirimedhi Institute of Science and Technology, Rayong 21210 Thailand

*Corresponding author, e-mail: vinich.p@vistec.ac.th

*Received 16 Oct 2024, Accepted 20 Apr 2025*
*Available online 28 May 2025*

**ABSTRACT**: Deep red to near-infrared organic light-emitting diodes (DR/NIR-OLEDs) have remarkably attracted much interest due to their potential applications in many areas. Herein, we present a simple structured near-infrared thermally activated delayed fluorescence (TADF) molecule (DMACCNBz) comprising a strong electron-accepting core (A) of 5,6-dicyano[2,1,3]benzothiadiazole (CNBz) end-capped with highest-energy molecular orbital (HOMO), rigid structure, and two strong electron donors (D) of 9,9-dimethyl-9,10-dihydroacridine (DMAC), thereby formulating a D-A-D type chromophore. The experimental and theoretical studies confirm that DMACCNBz is a TADF fluorophore with NIR emission ($\lambda_{\text{PL}} = 738$ nm) and a small singlet-triplet splitting energy ($\Delta E_{\text{ST}}$) of 0.07 eV. DMACCNBz is successfully applied as an emissive material in DR/NIR-OLEDs. The device using DMACCNBz 10 wt% doped emissive layer demonstrates a record-setting external quantum efficiency (EQE) of 7.19% with an emission peak at 696 nm, while the device using 30 wt% doping of DMACCNBz exhibits NIR emission with a peak at 722 nm, an EQE of 4.93%, and a maximum radiance of 4720 mW $\text{sr}^{-1}\text{m}^{-2}$.

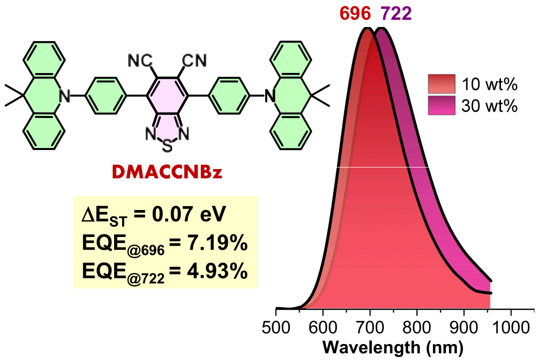

**KEYWORDS**: thermally activated delayed fluorescence, dicyano benzothiadiazole, dimethyl dihydroacridine, near-infrared chromophore, organic light-emitting diode

## INTRODUCTION

The deep red (DR) to near-infrared (NIR) light (700 nm $< \lambda <$ 2500 nm) has received significant attention due to its extensive applications in science and technology. These applications include telecommunications [1], photodynamic/photothermal therapies [2,3], biosensors [4], security applications [5], and organic light-emitting diodes (OLEDs) [6]. Particularly, NIR-OLEDs, when compared to their visible light-emitting counterparts, still encounter the challenge of small luminous efficiency and external quantum efficiency (EQE) due to the combination of the low photoluminescence quantum yield (PLQY) of NIR fluorophore and its inherent large non-radiative transition rate according to the widely known "Energy Gap Law" [7]. In general, organic NIR-emitting materials often feature rigid and highly conjugated backbones or strong push-pull characteristics to produce low band gaps, which instinctively brings about excessive interactions between the conjugated skeleton and other molecules, giving rise to low PLQY. Furthermore, conventional NIR fluorophores can only harvest the singlet excited state for light emission and waste the majority of the triplet excited state, limiting the internal quantum efficiency (IQE) to 25% or the device's maximum EQE of only 5%. Over the past decades, the thermally activated delayed fluorescence (TADF) mechanism has emerged as a

---

[†] 2021 Outstanding Scientist of Thailand.

promising alternative to conventional fluorescence because it utilizes both triplet and singlet states, allowing for 100% IQE. The TADF characteristic features a small energy gap ($\Delta E_{\mathrm{ST}} < 0.3$ eV) between the first singlet ($S_1$) and triplet ($T_1$) states, allowing the $T_1$ state to effectively undergo reverse intersystem crossing (RISC) to $S_1$ through thermal activation at room temperature [8, 9]. Since the pioneering report of purely organic TADF emitter-based OLEDs by Adachi et al in 2012 [10], the field of TADF OLEDs has considerably advanced, particularly in the development of high-performance TADF emitters. Recently, the numbers of NIR TADF emitters for NIR-OLEDs have been wisely investigated [11]. However, their performances have not yet met the level of the visible light-emitting TADF devices. The high-performance NIR TADF OLEDs need to be developed and new NIR TADF molecules should have been developed. Generally, TADF molecules are constructed with a donor-acceptor (D-A)-type rigid molecular architecture. A suitable twist angle and sufficient distance between the two moieties can interrupt and control the $\pi$-conjugation regulating a spatial separation of the highest occupied molecular orbital (HOMO) and the lowest unoccupied molecular orbital (LUMO), resulting in a small $\Delta E_{\mathrm{ST}}$ for an efficient RISC process. One common approach to achieve TADF with NIR emission is to narrow the HOMO-LUMO gap of the D-A molecule by shallowing the HOMO and/or lowering the LUMO, which could be managed by using a strong acceptor and strong donor couples. Several donor groups, including carbazole [12], acridine [13], triphenylamine (TPA) [14], and phenothiazine [15], have shown a strong donor strength with higher-lying HOMO and have been employed in the construction of NIR TADF molecules. However, the choices of acceptor units are quite limited when it comes to designing deep LUMO. Wang et al [16] reported the first organic DR/NIR-TADF molecule (TPA-DCPP) comprising 2,3-dicyanopirazino phenanthrene (DCPP) as the A unit end-capped with TPA as the D unit. The molecule presented a D-A-D structure with large and rigid $\pi$-conjugation with a LUMO value of $-3.52$ eV and DR/NIR emission at 588 nm. The non-doped OLED exhibited emission in the NIR region at 710 nm, and the doped device showed a high EQE of 9.8% with electroluminescent (EL) emission at 668 nm. Further extending the $\pi$-conjugated system of the DCPP acceptor resulted in 3,6-bis(4-(diphenylamino)phenyl)dibenzo[*a*, *c*]pyrazine-11,12-dinitrile (DPA-Ph-DBPzDCN) TADF molecule with a deeper LUMO value at $-3.63$ eV and DR/NIR emission at 618 nm [17]. Its doped device emitted at 732 nm with an EQE of 2.40%. Adachi et al [18] have developed dibenzo[a,c]phenazine-2,3,6,7-tetracarbonitrile (PZTCN) acceptor-based DR/NIR TADF emitter (TPA-PZTCN). The molecule showed DR/NIR emission at 674 nm with a LUMO level of $-3.84$ eV. The doped OLED achieved a deeper NIR emission with a peak at 734 nm and an EQE of 13.4%. The presence of four electron-withdrawing cyano groups in the acceptor unit of the molecule not only benefits its NIR emission but also can suppress non-radiative transitions through strong intermolecular interactions, giving rise to a high PLQY. Besides, there were more acceptors based on pyrazine carbonitrile have been investigated such as acenaphtho[1,2-*b*]pyrazine-8,9-dicarbonitrile (APDC) [19], acenaphtho[1,2-*b*] pyrazine-8,9-dicarbonitrile (AP) [20], acenaphtho[1,2-*b*]quinoxaline-8,9-dicarbonitrile (AQ) [19], anthryleno[1,2-*b*]pyrazine-2,3-dicarbonitrile (DCPA) [21], quinoxaline-6,7-dicarbonitrile (QCN) [22], 2,3-dicyanopyrazino phenanthroline (CNPP) [23], and dibenzo-[*a*, *c*]phenazine-3,6-dicarbonitrile (PZCN) [24]. Their corresponding DR/NIR TADF molecules have been synthesized and demonstrated moderate performances in the doped and non-doped devices. However, the synthesis of these pyrazine carbonitrile-based acceptors required sophisticated synthetic processes, making their commercialization and practical applications difficult. Recently, our group has presented a simple and strong electron-deficient acceptor based on 5,6-dicyano-[2,1,3]benzothiadiazole (CNBz) for the construction of NIR TADF dye [25]. CNBz presented an extremely strong accepting ability due to a combination of the extended $\pi$-conjugation system of benzothiadiazole and two electron-withdrawing cyano substituents. By end-capping CNBz with two TPA donors formulating a D-A-D molecule, TPACNBz realized an efficient DR/NIR emission at 674 nm with a deep LUMO level of $-3.70$ eV. The doped OLED emitted a NIR emission at 712 nm with a high maximum radiance of 10020 mW $\mathrm{sr}^{-1}\mathrm{m}^{-2}$ and an EQE of 6.57%.

To advance on this CNBz-based DR/NIR molecule, in this work, we further functionalized CNBz with a more rigid and stronger donor 9,9-dimethyl-9,10-dihydroacridine (DMAC) than TPA unit. DMAC has been known to exhibit a strong electron-donating property and a high HOMO level at $-4.90$ eV [11, 26]. Moreover, its locked biphenyl bridge structure could enhance molecular rigidity and reduce non-radiative decay, giving rise to high PLQY [27]. Currently, DMAC derivatives have attracted great attention owing to their good hole transporting ability, the practicality of their derivatives, and promising results for OLEDs [28]. Therefore, a simple structured DR/NIR molecule of DMACCNBz bearing CNBz end-capped with DMAC was designed and synthesized (Scheme 1). DMACCNBz with a twisted D-A-D type molecular structure presented a low HOMO-LUMO gap with a small $\Delta E_{\mathrm{ST}}$ of 0.07 eV. Its doped OLED showed DR/NIR emissions (696–722 nm) with EQEs of 4.93–7.19%.

## MATERIALS AND METHODS

All reagents and solvents were commercially purchased and used without further purification means unless otherwise noted. $^1$H- and $^{13}$C-NMR spectra were recorded using a 600 MHz Bruker AVANCE III HD (Rheinstetten, Germany) with $CDCl_3$ as a solvent in all cases. High-resolution mass spectrometry (HRMS) analysis was performed using a Bruker Autoflex MALDI-TOF mass spectrometer (Breman, Germany). UV-Vis absorption spectra were recorded using a PerkinElmer Lambda 1050 UV/Vis/NIR spectrometer (Waltham, MA, USA). Photoluminescence spectra and photoluminescence decay profiles were studied using an Edinburgh Instruments FLS980 spectrometer (Livingston, UK). The absolute PLQY was measured using an integrating sphere combined with Edinburgh Instruments FLS980 (Livingston, UK). Thermogravimetric analysis (TGA) was recorded using a Rigaku STA8122 thermogravimetric analyzer (Tokyo, Japan) while flushing with nitrogen at a heating rate of 10 °C/min. Melting points were measured using a Kruss KSP1N melting point meter (Hamburg, Germany) and the values were uncorrected. The electrochemical experiment was operated on Autolab PGSTAT101 (Metrohm Autolab BV, Utrecht, The Netherlands) using a three-electrode system (Pt as a counter electrode; glassy carbon as a working electrode; Ag/AgCl as a reference electrode). The samples (0.1 M) were dissolved in dry dichloromethane ($CH_2Cl_2$) containing tetrabutylammonium hexafluorophosphate ($n$-$Bu_4NPF_6$) ($10^{-3}$ M) as a supporting electrolyte and analyzed at a scan rate of 50 mV/s under argon. Single-crystal X-ray diffraction (SC XRD) was performed using a Bruker D8 Venture single-crystal diffractometer (Karlsruhe, Germany) at 100 K (Mo K$\alpha = 0.7107$ Å). The crystal refinement was calculated and illustrated using APEX4, PLATON, OLEX1.5, and MERCURY3 software. Crystallographic data deposited at the Cambridge Crystallographic Data Centre under CCDC 2371981 of DMACCNBz contains supplementary crystallographic data, including the structure factors, respectively. This data can be obtained free of charge via www.ccdc.cam.ac.uk.

The quantum chemical calculations were performed using the Gaussian 16 package [29]. The ground state geometries, HOMO/LUMO distributions, and energy levels were executed by using density functional theory (DFT) calculation at the B3LYP/6-31G(d,p) level of theory in the gas phase. The singlet and triplet excited states were calculated using a time-dependent (TD)-DFT B3LYP/6-31G(d,p) basis set.

OLED devices with the structure of indium tin oxide (ITO)/1,4,5,8,9,11-hexaazatriphenylene hexacarbonitrile (HAT-CN) (8 nm)/N,N′-bis(naphthalen-1-yl)-N,N′-bis(phenyl)-benzidine (NPB) (30 nm)/4,4′,4-tris(carbazol-9-yl)triphenylamine (TCTA) (10 nm)/DMACCNBz doped 4,4′-bis(N-carbazolyl)-1,1′-biphenyl (CBP) (30 nm)/1,3,5-tri(m-pyrid-3-yl-phenyl)-benzene (TmPyPB) (40 nm)/lithium fluoride (LiF) (1 nm)/aluminum (Al) (100 nm) were fabricated on patterned indium tin oxide (ITO) glass substrates with a sheet resistance of 12 Ω/sq. The substrates were thoroughly pre-cleaned by ultrasonic treatment in liquinox detergent, deionized water, acetone, and isopropanol and brewed with nitrogen for drying. They were then cured with UV/Ozone for 20 min before use. The OLEDs were fabricated using a Kurt J. Lasker mini SPECTROS 100 thin film deposition system (Kurt J. Lesker, Jefferson Hills, USA) under vacuum conditions with a base pressure lower than $1 \times 10^{-5}$ bar to form an active diode area of 4 mm$^2$. Thermal evaporation rates were 0.2–0.4 Å/s for HATCN, NPB, TCTA, DMACCNBz:CBP, and TmPyPB layers, 0.05–0.1 Å/s for LiF layer, and about 1 Å/s for the Al layer. The film thickness was monitored using a quartz oscillator thickness sensor. The absolute EQE of OLEDs was obtained using a Hamamatsu Photonic C9920-12 External Quantum Efficiency Measurement System (Hamamatsu, Japan) utilizing and an integrating sphere under an ambient atmosphere at room temperature. Hole- and electron-only devices (ITO/-magnesium fluoride ($MgF_2$) (20 nm)/DMACCNBz (100 nm)/molybdenum oxide ($MoO_3$) (3 nm)/Al (100 nm) and ITO/$MgF_2$ (20 nm)/DMACCNBz (100 nm)/LiF (1 nm)/Al (100 nm)) were fabricated and measured as mentioned above. Current density-voltage-luminescence (*J-V-L*) characteristics were measured by using a Keithley 2400 source meter and a Hamamatsu Photonics PMA-12 multi-channel analyzer.

*Synthesis of 4,7-bis(4-(9,9-dimethylacridin-10(9H) -yl) phenyl)-5, 6-difluorobenzo [c][1,2,5] thiadiazole (FDMACBz)*: A mixture of 4, 7-dibromo-5, 6-difluoro-2,1-3-benzothiadiazole (0.062 g, 0.188 mmol), 9,9-dimethyl-10-(4-(4,4,5,5-tetramethyl-1,3, 2-dioxaborolan-2-yl)phenyl)-9,10-dihydroacridine (0.170 g, 0.143 mmol), $Pd(PPh_3)_4$ (0.01 g, 0.093 mmol), and 2 M $Na_2CO_3$ (12 ml) in dry THF (20 ml) was degassed under nitrogen atmosphere. The reaction mixture was stirred and heated at reflux for 48 h, then cooled to room temperature. Water (50 ml) was added and the mixture was extracted with $CH_2Cl_2$ ($3 \times 50$ ml). The organic layer was combined, washed with water, brine, dried over anhydrous $Na_2SO_4$, filtered, and concentrated in a vacuum. Purification by column chromatography on silica gel eluting with hexane:$CH_2Cl_2$ (3:1) gave yellow solids (113 mg, 63%). M.p. >360 °C; $^1$H NMR (600 MHz, $CDCl_3$) $\delta$ 8.17 (d, $J$ = 7.9 Hz, 2H), 7.58 (d, $J$ = 7.8 Hz, 2H), 7.52–7.47 (m, 2H), 7.04 (t, $J$ = 7.7 Hz, 2H), 6.97 (t, $J$ = 7.4 Hz, 2H), 6.46 (d, $J$ = 8.2 Hz, 2H), 1.73 (s, 6H); $^{13}$C NMR (151 MHz, $CDCl_3$) $\delta$ 142.1, 140.7, 133.1, 131.4, 130.2, 130.0, 126.4, 125.2, 120.8, 114.2, 36.0, 31.19; HRMS MALDI-TOF ($m/z$): calcd for $C_{50}H_{36}N_6S$ 738.2629; found: 738.2621 [M+].

*Synthesis of 4,7-bis(4-(9,9-dimethylacridin-10(9H) -yl) phenyl) benzo [c][1,2,5] thiadiazole-5, 6-dicarbonitrile (DMACCNBz)*: FDMACBz (107 mg, 0.15 mmol), KCN (75 mg, 1.16 mmol), and 18-crown-6 (1.5 mg, 0.006 mmol) were added to a Schlenk tube, then dried by heating gun before being flushed with argon. Dried THF (2 ml) was added and degassed. The reaction mixture was stirred under argon at reflux for 20 h. The mixture was poured into water and then extracted with $CH_2Cl_2$ (3 × 20 ml). The combined organic layer was washed with water, brine, dried over anhydrous $Na_2SO_4$, filtered, and concentrated in a vacuum. Purification by column chromatography on silica gel eluting with hexane:$CH_2Cl_2$ (3:2) followed by reprecipitation in a mixture of $CH_2Cl_2$ and methanol gave deep red solids (103 mg, 65%). M.p. >360 °C; $^1$H NMR (600 MHz, $CDCl_3$) $\delta$ 8.12 (d, $J$ = 8.2 Hz, 2H), 7.65 (d, $J$ = 8.2 Hz, 2H), 7.50 (dd, $J$ = 7.8, 1.5 Hz, 2H), 7.07–7.05 (m, 2H), 6.99 (td, $J$ = 7.4, 1.2 Hz, 2H), 6.46 (d, $J$ = 8.1 Hz, 2H), 1.72 (s, 6H); $^{13}$C NMR (151 MHz, $CDCl_3$) $\delta$ 154.3, 144.0, 141.1, 140.6, 133.0, 132.1, 131.5, 130.8, 126.6, 125.3, 121.2, 115.3, 114.5, 113.0, 36.1, 31.0; HRMS MALDI-TOF ($m/z$): calcd for $C_{50}H_{36}N_6S$ 752.2722; found: 752.2761 [M+].

## RESULTS AND DISCUSSION

The synthesis of the designed TADF molecule DMACCNBz was accomplished in two steps, as outlined in Scheme 1. Suzuki cross-coupling reaction of 4,7-dibromo-5,6-difluorobenzo[$c$][1,2,5] thiadiazole and 9,9-dimethyl-10-(4-(4,4,5,5-tetramethyl-1, 3, 2-dioxaborolan-2-yl) phenyl)-9, 10-dihydroacridine catalyzed by $Pd(Ph_3P)_4/Na_2CO_3$ followed by nucleophilic substitution reaction of the resultant FDMACBz with KCN in the presence of 18-crown-6 afford produced DMACCNBz as deep red solids in a moderate yield. The chemical structures of the synthesized molecules were unambiguously characterized by $^1$H-NMR, $^{13}$C-NMR, HRMS MALDI-TOF (Fig. S1), while the molecular structure of DMACCNBz was further proved by single crystal X-ray diffraction.

A suitable single crystal of DMACCNBz was grown via a slow diffusion of methanol into a $CH_2Cl_2$ solution. The precise geometry was confirmed via SC XRD measurements, and the corresponding crystallographic data are provided in Table S1. The crystal structure of DMACCNBz (Fig. S2) is a monoclinic $P2_{1/n}$ space-group ($a$ = 7.0601(6) Å], $b$ = 13.1064(11) Å, $c$ = 42.680(3) Å). It was observed that the plane of the phenyl ring and the plane of the DMAC unit were nearly perpendicular to each other, indicating significant steric repulsion between them. The structure reveals a twisted conformation with large torsion angles of 66.6° and 86.6° between the CNBz acceptor and the phenyl ring and between the DMAC donor and the phenyl ring, respectively, as depicted in Fig. S1. These large torsion angles could facilitate the separation of HOMO and LUMO distributions, contributing to the observed small $\Delta E_{ST}$.

To gain insight into the electronic property of DMACCNBz, DFT calculations were performed using the B3LYP/6-31G(d) and TDA-B3LYP/6-31G(d) in gas phase for the ground state and excited state properties, respectively. As shown in Fig. 1, the optimized geometry of DMACCNBz shows dihedral angles of 80.0° and 52.6° between the phenyl ring and its adjacent end-capping DMAC and central CNBz units, respectively. According to such large dihedral angles, the electron distribution of HOMO was mainly on the two electron-donating DMAC moieties, while the electron of LUMO was localized on the electron-accepting CNBz core with tiny electron distribution on nearby phenyl rings. These HOMO and LUMO orbitals display a small overlap which could lead to comparable energy levels for $S_1$ and $T_1$, resulting in small $\Delta E_{ST}$ values. The calculated HOMO and LUMO energies revealed an energy gap ($\Delta E$) of 1.10 eV matching well with the NIR emission. This could benefit from strong electron-donating and strong electron-deficient characters of the DMAC and CNBz building blocks, respectively, and its D-A-D structure. The excited state calculations of DMACCNBz estimated the $\Delta E_{ST}$ value to be 0.001 eV, which is sufficiently low to facilitate efficient RISC at room temperature.

The optical properties of DMACCNBz were investigated using UV-Vis absorption and photoluminescence spectroscopy in dilute solution and thin film, as shown in Fig. 2 and listed in Table 1. The UV-Vis absorption spectrum in solution displayed absorption peaks at 286 nm assigned to the $\pi$-$\pi^*$ transition of DMAC unit, at 378 nm attributed to the $\pi$-$\pi^*$ transition of conjugate backbone, and at 522 nm ascribed to the intramolecular charge transfer (ICT) from DMAC donor to CNBz acceptor. The latter band was broad with a low molar extinction coefficient ($\varepsilon = 1.2 \times 10^3$ $M^{-1}cm^{-1}$), indicating a weak charge transfer (CT) characteristic, agreeing well with the spatially separating HOMO and LUMO orbitals observed. DMACCNBz in solution showed NIR emission with a broad CT emission band peaked at 378 nm. This CT emission characteristic was further evaluated by a solvatochromic study, revealing that the PL spectra displayed solvent polarity-dependent profiles, where the PL peaks red-shifted from 740 nm in low polarity toluene solution to 861 nm in high polarity $CH_2Cl_2$ (Fig. 2b). As depicted in Fig. 2c, the molecule in the thin film exhibited UV-Vis absorption and PL profiles similar to its solution. The film showed NIR emission with a peak at 750 nm and a PLQY value of 1.3%. The transient PL decay spectra at 300 K of DMACCNBz film exhibited distinct double exponential decay components over 200 µs, with the

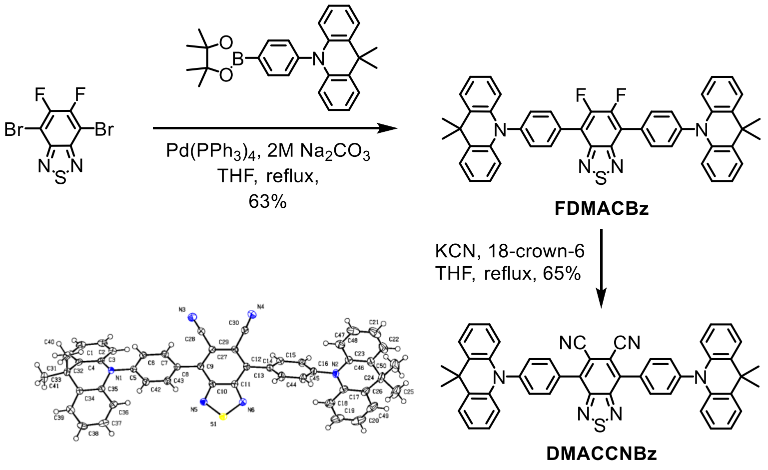

**Scheme 1** Synthesis of DMACCNBz and its single crystal structure.

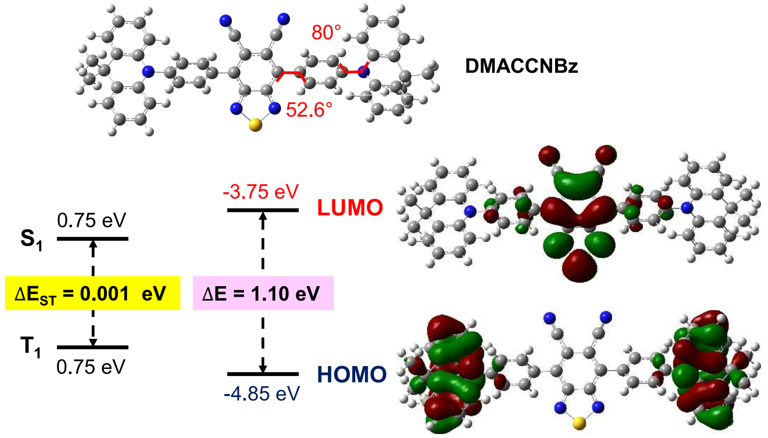

**Fig. 1** Optimized geometry, HOMO/LUMO orbitals and energies, lowest-lying singlet ($S_1$), and lowest-lying triplet ($T_1$) energy levels calculated by B3LYP/6-31G(d) and TDA-B3LYP/6-31G(d) methods.

delayed fluorescence (DF) component decaying with a half-life of ~5 µs. The half-life of the prompt fluorescence (PF) component was estimated to be 8 ns over the time range of 100 ns, corresponding to the $S_1$ relaxation to the $S_0$ (Figs. 2d and S2).

To further validate the TADF characteristic of DMACCNBz, a series of experiments were conducted. Firstly, it can be verified by an oxygen quenching experiment. This method relies on the assumption that TADF is quenched by molecular oxygen under oxygen-saturated conditions and only PF is observed. As shown in Fig. 3a, the PL intensity of DMACCNBz in toluene solution in the absence of oxygen (degassed) is more than doubled compared to that of the aerated condition, confirming the existence of TADF emission in this compound. Secondly, it is the determination

**Table 1** Key optical and physical data of DMACCNBz.

| $\lambda_{em}$ (nm) sol[a]/film[b]/dfilm | $\tau$ (ns)[e] sol[a]/film[b] | PLQY (%)[i] sol[a]/film[b]/dfilm | $E_g^{opt}/E_g^{elec}$[j] (eV) | HOMO/LUMO[k] (eV) | $E_S/E_T/\Delta E_{ST}$[l] (eV) |
|---|---|---|---|---|---|
| 738/750/675[c] (708)[d] | 6[f](10)[g]/14[h](4940)[i] | 1.6/1.3/36[c] (16)[d] | 1.82/1.91 | −5.40/−3.49 | 2.26/2.19/0.07 |

[a] Measured in toluene solution. [b] Measured in neat film. [c] Measured from 10 wt% DMACCNBz:CBP doped film. [d] Measured from 30 wt% DMACCNBz:CBP doped film. [e] Transient PL decay time. [f] Aerated solution. [g] Degassed solution. [h] Prompt fluorescence (PF). [i] Delayed fluorescence (DF). [j] Estimated from absorption onset of thin film: $E_g^{opt} = 1240/\lambda_{onset}$ and from CV: $E_g^{opt} = E_{ox}^{onset} - E_{re}^{onset}$. [k] HOMO $= -(4.44 + E_{ox}^{onset})$ and LUMO = HOMO + $E_g^{opt}$. [l] Singlet ($S_1$) and triplet ($T_1$) excited state is estimated from onsets of prompt PL and delayed PL spectra of 2 wt% DMACCNBz:PMMA doped film and $\Delta E_{ST} = E_S - E_T$.

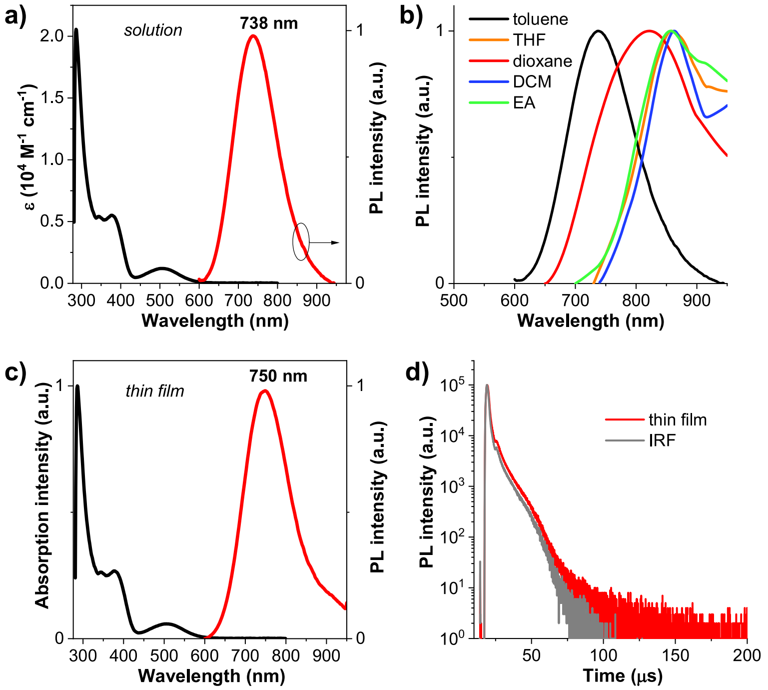

**Fig. 2** UV-VIS absorption and PL spectra of DMACCNBz in (a) toluene solution and (c) thin film coated on fused silica substrate. (b) PL spectra of DMACCNBz in different solvents. (d) Transient PL decay trace of thin film over a time range of 200 μs.

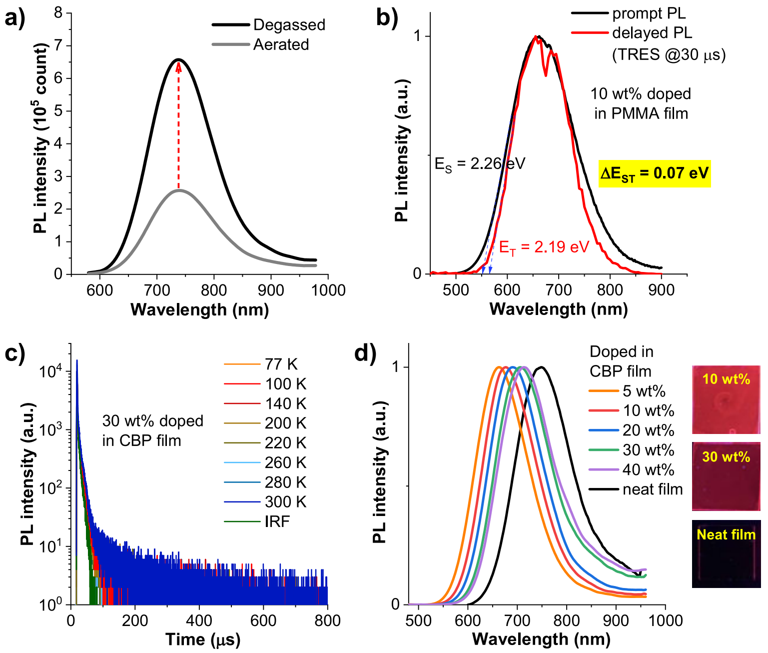

**Fig. 3** (a) PL spectra of aerated and degassed 10 wt% DMACCNBz:PMMA film covered with EXCEVAL™ film. (b) TRES of 2 wt% DMACCNBz:PMMA film covered with EXCEVAL™ film. (c) Temperature-dependent transient PL decay traces of 30 wt% DMACCNBz:CBP film from 77 to 300 K. (d) PLspectra of DMACCNBz neat film and DMACCNBz:CBP films at different doping concentrations (insert: images of films under UV light 365 nm illumination).

of $\Delta E_{ST}$, the most important parameter in verifying a TADF molecule, which can be directly estimated from prompt PL and phosphorescence spectra. The time-resolved emission spectrum (TRES) measurement of 10 wt% DMACCNBz doped in polymethyl methacrylate (PMMA) thin film covered with an EXCEVAL™ film was carried out. As depicted in Fig. 3b, the spectra of the prompt PL (TRES slice @100 ns after flash) and delayed PL (TRES slice @30 µs after flash) are nearly identical, suggesting that the delayed component is DF. In general, the phosphorescence from the $T_1$ state will appear at a longer wavelength than the fluorescence because of the lower-lying energy of the $T_1$ state. Accordingly, the $\Delta E_{ST}$ was estimated from the onset of the two spectra to be 0.07 eV. This narrow $\Delta E_{ST}$ would ensure an efficient upconversion from $T_1$ to $S_1$ or TADF process at room temperature. The third method is to verify the origin of the delayed component by measuring the temperature dependence of the emission decay. The temperature-dependent transient PL spectra of 30 wt% DMACCNBz doped in CBP film were evaluated over a temperature range of 77 K to 300 K. As shown in Fig. 3c, the delay component is seriously suppressed when the film is cooled to 77 K and gradually increased with the temperature elevated, indicating that the delayed component originates from a thermally activated process. These results prove the assignment of the delayed component as TADF.

To achieve an enhanced TADF emission, the TADF molecule typically needs to be doped in a suitable host material to stabilize its $T_1$ state, enlarge the interaction distance, and suppress the annihilations. CBP was identified as a suitable host matrix for deep-red and NIR emitters due to its high triplet energy and appropriate HOMO/LUMO levels [30, 31]. The PL spectra and PLQYs were therefore investigated in 5–40 wt% doped films of DMACCNBz in a CBP matrix, as shown in Fig. 3d. The PL exhibited a continuing blue shift in emissions as doping concentrations decreased compared to the neat film. At 10 wt% doping concentration, the film displayed a DR emission with a peak at 675 nm, while at 30 wt% doping concentration, the film emitted a NIR emission with a peak at 708 nm. The PLQY values of the thin films were significantly improved from 1.6% for the neat film to 36% for 10 wt% doped film and 16% for 30 wt% doped film (Table 1), indicating that dispersion of DMACCNBz in a CBP host matrix could alleviate the aggregation-caused quenching problem to a large extent and endowed TADF emission

The thermal property of DMACCNBz was analyzed by TGA, which showed a high decomposition temperature ($T_{5d}$) at a 5% weight loss of 428 °C (Fig. 4a). This suggests that DMACCNBz has superior thermal

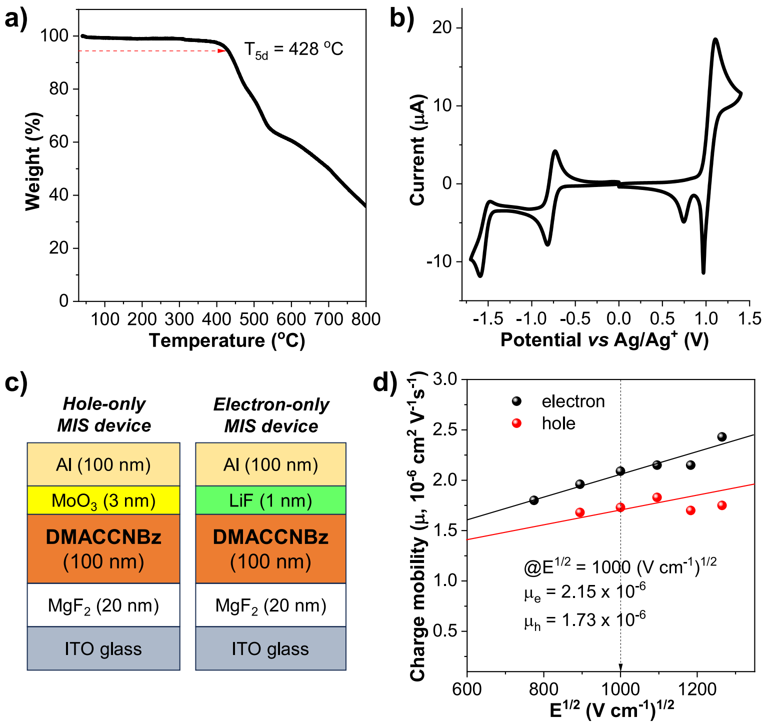

**Fig. 4** (a) TGA thermogram measured at a heating rate of 10 °C/min under $N_2$ flow. (b) CV voltammogram analyzed in $CH_2Cl_2$/*n*-$Bu_4NPF_6$ at a scan rate of 50 mV/s under argon. (c) The structures of hole-only and electron-only MIS devices. (d) Electric-field dependence of the charge mobility plots.

stability and is capable of fabricating thin film using the thermal evaporation technique, beneficial to a stable and efficient device. The electrochemical property of DMACCNBz was investigated by cyclic voltammetry (CV) experiment conducted in a dry $CH_2Cl_2$ solution containing $n$-$Bu_4NPF_6$ as a supporting electrolyte. As depicted in Fig. 4b, the CV trace reveals a bipolar redox feature. Two distinct quasi-reversible reductions at half-wave potentials ($E_{1/2}$) of −0.85 V and −1.62 V were assigned the formation of radical anions of the electron-withdrawing CN [32] and Bz [33, 34] acceptor, respectively, while two oxidation waves at the potential of 0.74 V and $E_{1/2}$ of 0.96 V. The first oxidation was attributed to the formation of radical cations of the electron-donating DMAC moiety [26, 35, 36]. Accordingly, the electrochemical bandgap ($E_g^{ele}$) of DMACCNBz was calculated from the onset of oxidation and reduction to be 1.82 eV, which is slightly lower than the optical bandgap ($E_g^{opt} = 1.91$ eV) estimated from the absorption onset of the solid film due to the exciton binding energy. Based on the onset of oxidation ($E_{ox}^{onset}$), the HOMO level was calculated to be −5.40 eV from HOMO $= -(4.44 + E_{ox}^{onset})$ and the LUMO level was further deduced from HOMO and $E_g^{opt}$ to be −3.49 eV from LUMO = HOMO + $E_g^{opt}$. The LUMO value is comparable to TPACNBz [24], due to their shared electron-withdrawing core. Since charge carrier mobility of emissive material is one of the key parameters to achieve efficient devices, the hole ($\mu_h$) and electron ($\mu_e$) mobilities of DMACCNBz were measured using metal-insulator-semiconductor (MIS) diodes in combination with the charge extraction in linearly increasing voltage (CELIV) method (MIS-CELIV). The hole- and electron-only MIS devices were fabricated with the following configurations ITO/$MgF_2$ (20 nm)/DMACCNBz (100 nm)/$MoO_3$ (3 nm)/Al (100 nm) and ITO/$MgF_2$ (20 nm)/DMACCNBz (100 nm)/LiF (1 nm)/Al (100 nm), respectively (Fig. 4c). As shown in Fig. 4d. the electric-field dependence of the charge mobility plots reveal $\mu_h$ and $\mu_e$ of DMACCNBz at 1000 $(\text{V cm}^{-1})^{1/2}$ to be $2.15 \times 10^{-6}$ $\text{cm}^2\text{V}^{-1}\text{s}^{-1}$ and $1.73 \times 10^{-6}$ $\text{cm}^2\text{V}^{-1}\text{s}^{-1}$, respectively. This indicates that DMACCNBz possesses a well-balanced charge-transporting property, leading to efficient device performance.

The EL performance of DMACCNBz as an emitting material was investigated in multilayer OLEDs with the optimized configurations of ITO/HATCN (8 nm)/NPB (30 nm)/TCTA (10 nm)/10–30 wt% DMACCNBz:CBP (30 nm)/TmPyPB (40 nm)/LiF (1 nm)/Al (100 nm) (Fig. 5). In these devices, ITO and Al served as anode and cathode, while HATCN and LiF acted as hole and electron injection layers, respectively. To balance holes and electrons and limit the recombination zone in the emissive layer (EML), NPB was applied as the hole-transporting layer (HTL), TCTA with its high LUMO energy level (2.3 eV) and poor $\mu_e$ ($10^{-8}$ $\text{cm}^{-2}\text{V}^{-1}\text{s}^{-1}$) was inserted as an electron blocking layer (EBL) [36]. TmPyPB functioned as the electron-transporting layer (ETL). 10 and 30 wt% DMACCNBz doped in CBP host were investigated as the EML. The corresponding EL characteristic plots are depicted in Fig. 6, and the key EL parameters are given in Table 2.

The OLED using 10 wt% DMACCNBz:CBP as an EML showed a DR emission with a peak at 696 nm corresponding to a Commission Internationale de I'Éclairage (CIE) coordinates of (0.67, 0.33). The device achieved remarkable EL performance with a low turn-on voltage ($V_{on}$) of 3.4 V, a maximum radiance of 7051 mW $\text{sr}^{-1}\text{m}^{-2}$, and a maximum EQE of 7.19%. The OLED fabricated with a higher doping concentration of DMACCNBz (30 wt%) exhibited NIR emission with a peak at 722 nm and a CIE coordinate of (0.69, 0.31). The device demonstrated a slightly lower EL performance with a $V_{on}$ of 4.2 V, a maximum radiance of 4720 mW $\text{sr}^{-1}\text{m}^{-2}$, and a maximum EQE of 4.93%. These results related well with the PLQY of the EML (Table 1). Additionally, the EL spectra of both devices displayed sole DMACCNBz emission consistent well with the PL spectra of the corresponding EML (Fig. 6c). There were no emissions from the host being observed, suggesting complete energy transfer from the CBP to DMACCNBz. The EL spectra endured stability within various applied voltages, as illustrated in Fig. S3, indicating excellent stability during the electrical charge injection process and exciton recombination well confined in the EML. Besides, DMACCNBz exhibited OLED performance comparable to its predecessor, TPACNBz [25]. The EL spectra of DMACCNBz showed a longer EL emission at 722 nm, compared to 712 nm for TPACNBz, with high efficiency. Accordingly, this outcome represents one of the top EL performances among thiadiazole-based derivatives for pure organic deep-red to NIR OLEDs with an emission peak exceeding 680 nm reported to date [38]. Moreover, these devices exhibit low-efficiency roll-off. Overall, this novel DMACCNBz emitter, through simple molecular engineering, demonstrates high-efficiency DR/NIR emissions, making it suitable for practical

**Table 2** Summary of device EL performance of the OLEDs.[a]

| EML | $V_{on}$ (V) | $\lambda_{EL}$ (nm) | $R_{max}$ (mW $\text{sr}^{-1}\text{m}^{-2}$) | $J_{max}$ (mA $\text{cm}^{-2}$) | EQE (%) | CIE (x,y) |
|---|---|---|---|---|---|---|
| 10 wt% DMACCNBz:CBP | 3.4 | 696 | 7051 | 255 | 7.19 | (0.67, 0.33) |
| 30 wt% DMACCNBz:CBP | 4.2 | 722 | 4720 | 209 | 4.93 | (0.69, 0.31) |

[a] ITO/HATCN (8 nm)/NPB (30 nm)/TCTA (10 nm)/EML (30 nm)/TmPyPB (40 nm)/LiF (1 nm)/Al (100 nm).

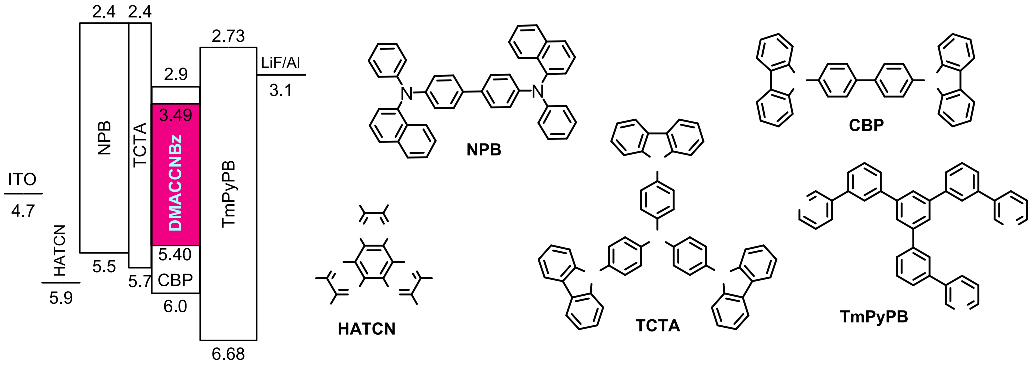

**Fig. 5** Energy level diagram of OLED and molecular structures of organic materials used in the device.

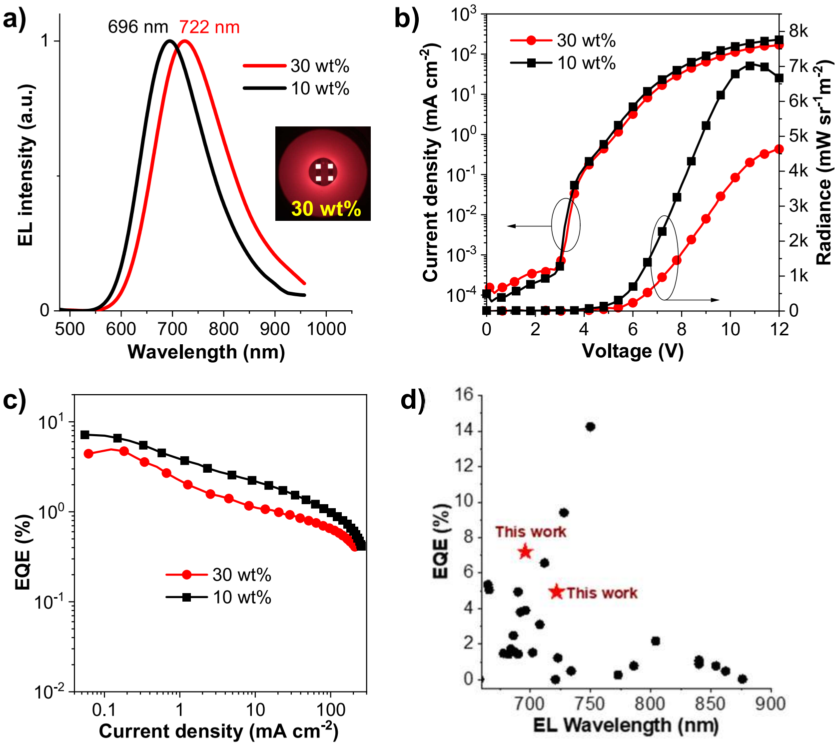

**Fig. 6** (a) Normalized EL spectra of the OLEDs (insert: image of OLED-based on 30 wt% DMACCNBz:CBP operated @9 V). (b) Current density-voltage-radiance (*J-V-R*) characteristics. (c) Current density-external quantum efficiency (*J-EQE*) plots. (d) EQE summary of the reported DR/NIR fluorescence OLEDs with an emission peak greater than 680 nm.

OLED applications.

## CONCLUSION

In summary, we have successfully designed and synthesized a NIR emissive TADF molecule DMACCNBz by integrating one CNBz as a strong electron-accepting core with two DMAC as strong electron-donating end-capping units, thereby formulating a D-A-D chromophore. DMACCNBz displays a TADF property with a narrow $\Delta E_{\mathrm{ST}}$ of 0.07 eV. The molecule exhibits NIR emission in both solution and thin film with well-balanced charge mobility and decent thermal stability. It could be beneficial from the use of a high electron-deficient CNBz unit. DMACCNBz is successfully employed as an emissive material in OLEDs. The devices based on DMACCNBz doped in CBP host emissive layers exhibit DR/NIR emissions with low $V_{\mathrm{on}}$ (3.4–4.2 V) and high EQE of 4.93–7.19%. This work demonstrates that an efficient NIR TADF molecule can be developed using a simple and extremely high electron-deficient CNBz as an acceptor core. We also anticipate that our design strategy would open up a new possibility for achieving low-bandgap organic semiconductor materials for other optoelectronic applications.

## Appendix A. Supplementary data

Supplementary data associated with this article can be found at https://dx.doi.org/10.2306/scienceasia1513-1874.2025.s011.

*Acknowledgements*: This work was financially supported by the National Research Council of Thailand (NRCT) (grant no. N42A650196).

## REFERENCES

1. Le ST, Kanesan T, Bausi F, Haigh PA, Rajbhandari S, Ghassemlooy Z, Papakonstantinou I, Popoola WO, et al (2014) 10 Mb/s visible light transmission system using a polymer light-emitting diode with orthogonal frequency division multiplexing. *Opt Lett* **39**, 3876–3879.
2. Liu J, Liang H, Li M, Luo Z, Zhang J, Guo X, Cai K (2018) Tumor acidity activating multifunctional nanoplatform for NIR-mediated multiple enhanced photodynamic and photothermal tumor therapy. *Biomaterials* **157**, 107–124.
3. Yuan H, Yang H, Yuan P, Wang T, Zhou Q (2023) Carbon quantum dots as drug carriers for tumor-associated macrophage repolarization following photothermal therapy. *ScienceAsia* **49**, 627–634.
4. Lochner CM, Khan Y, Pierre A, Arias AC (2014) All-organic optoelectronic sensor for pulse oximetry. *Nat Commun* **5**, 5745.
5. Lee EC, Jung H, Kim D (2011) New finger biometric method using near infrared imaging. *Sensors* **11**, 2319–2333.
6. Jeon Y, Choi H-R, Lim M, Choi S, Kim H, Kwon JH, Park K-C, Choi KC (2018) A wearable photobiomodulation patch using a flexible red-wavelength OLED and its *in vitro* differential cell proliferation effects. *Adv Mater Technol* **3**, 1700391.
7. Englman R, Jortner J (1970) The energy gap law for radiationless transitions in large molecules. *Mol Phys* **18**, 145–164.
8. Luo Y, Li S, Zhao Y, Li C, Pang Z, Huang Y, Yang M, Zhou L, et al (2020) An ultraviolet thermally activated delayed fluorescence OLED with total external quantum efficiency over 9%. *Adv Mater* **32**, 2001248.
9. Godumala M, Choi S, Cho MJ, Choi DH (2019) Recent breakthroughs in thermally activated delayed fluorescence organic light emitting diodes containing non-doped emitting layers. *J Mater Chem C* **7**, 2172–2198.
10. Uoyama H, Goushi K, Shizu K, Nomura H, Adachi C (2012) Highly efficient organic light-emitting diodes from delayed fluorescence. *Nature* **492**, 234–238.
11. Sharma S, Pal AK (2022) Recent advances of NIR-TADF ($\lambda_{\max}$PL/EL > 700 nm) emitters and their applications in OLEDs. *J Mater Chem C* **10**, 15681–15707.
12. Ledwon P (2019) Recent advances of donor-acceptor type carbazole-based molecules for light emitting applications. *Org Electron* **75**, 105422.
13. Chen T, Lu C-H, Huang C-W, Zeng X, Gao J, Chen Z, Xiang Y, Zeng W, et al (2019) Tuning the emissive characteristics of TADF emitters by fusing heterocycles with acridine as donors: highly efficient orange to red organic light-emitting diodes with EQE over 20%. *J Mater Chem C0* **7**, 9087–9094.
14. Xiao Y, Wang H, Xie Z, Shen M, Huang R, Miao Y, Liu G, Yu T, et al (2022) NIR TADF emitters and OLEDs: challenges, progress, and perspectives. *Chem Sci* **13**, 8906–8923.
15. Wang B, Qiao X, Yang Z, Wang Y, Liu S, Ma D, Wang Q (2018) Realizing efficient red thermally activated delayed fluorescence organic light-emitting diodes using phenoxazine/phenothiazine-phenanthrene hybrids. *Org Electron* **59**, 32–38.
16. Wang S, Yan X, Cheng Z, Zhang H, Liu Y, Wang Y (2015) Highly efficient near-infrared delayed fluorescence organic light emitting diodes using a phenanthrene-based charge-transfer compound. *Angew Chemie Int Ed* **54**, 13068–13072.
17. Wang S, Miao Y, Yan X, Ye K, Wang Y (2018) A dibenzo[$a,c$]phenazine-11,12-dicarbonitrile (DBPzDCN) acceptor based thermally activated delayed fluorescent compound for efficient near-infrared electroluminescent devices. *J Mater Chem C* **6**, 6698–6704.
18. Balijapalli U, Nagata R, Yamada N, Nakanotani H, Tanaka M, D'Aléo A, Placide V, Mamada M, et al (2021) Highly efficient near-infrared electrofluorescence from a thermally activated delayed fluorescence molecule. *Angew Chemie Int Ed* **60**, 8477–8482.
19. Yuan Y, Hu Y, Zhang Y-X, Lin J-D, Wang Y-K, Jiang Z-Q, Liao L-S, Lee S-T (2017) Over 10% EQE near-infrared electroluminescence based on a thermally activated delayed fluorescence emitter. *Adv Funct Mater* **27**, 1700986.
20. Xue J, Liang Q, Wang R, Hou J, Li W, Peng Q, Shuai Z, Qiao J (2019) Highly efficient thermally activated delayed fluorescence via J-aggregates with strong intermolecular charge transfer. *Adv Mater* **31**, 1808242.
21. Yu Y-J, Hu Y, Yang S-Y, Luo W, Yuan Y, Peng C-C, Liu J-F, Khan A, et al (2020) Near-infrared electroluminescence beyond 800 nm with high efficiency and radiance from anthracene cored emitters. *Angew Chemie Int Ed* **59**, 21578–21584.
22. Li C, Duan R, Liang B, Han G, Wang S, Ye K, Liu Y, Yi Y, Wang Y (2017) Deep-red to near-infrared thermally activated delayed fluorescence in organic solid films and electroluminescent devices. *Angew Chemie Int Ed* **56**, 11525–11529.
23. Wang H, Zhao B, Qu C, Duan C, Li Z, Ma P, Chang P, Han C, et al (2022) 2,3-Dicyanopyrazino phenanthroline enhanced charge transfer for efficient near-infrared thermally activated delayed fluorescent diodes. *Chem Eng J* **436**, 135080.
24. Zhang Y-L, Ran Q, Wang Q, Liu Y, Hänisch C, Reineke S, Fan J, Liao L-S (2019) High-efficiency red organic light-emitting diodes with external quantum efficiency close to 30% based on a novel thermally activated delayed fluorescence emitter. *Adv Mater* **31**, 1902368.
25. Kumsampao J, Chaiwai C, Chasing P, Chawanpunyawat T, Namuangruk S, Sudyoadsuk T, Promarak V (2020) A simple and strong electron-deficient 5,6-dicyano[2,1,3]benzothiadiazole-cored donor-acceptor-donor compound for efficient near infrared thermally activated delayed fluorescence. *Chem An Asian J* **15**, 3029–3036.
26. Braveenth R, Kim K, Bae I-J, Raagulan K, Kim BM, Kim M, Chai KY (2021) Acridine based small molecular hole transport type materials for phosphorescent OLED application. *Molecules* **26**, 7680.

27. He Z, Li J, Liu D, Mei Y, Wan H (2023) Performance enhancement in thermally activated delayed fluorescence emitters by multi-fold layout. *Dye Pigment* **212**, 111104.
28. Zhang Q, Li B, Huang S, Nomura H, Tanaka H, Adachi C (2014) Efficient blue organic light-emitting diodes employing thermally activated delayed fluorescence. *Nat Photonics* **8**, 326–332.
29. Frisch MJ, Trucks GW, Schlegel HB, Scuseria GE, Robb MA, Cheeseman JR, Scalmani G, Barone V, et al (2016*) Gaussian 16* Rev. C.01.
30. Data P, Pander P, Okazaki M, Takeda Y, Minakata S, Monkman AP (2016) Dibenzo[a,j]phenazine-cored donor-acceptor-donor compounds as green-to-red/NIR thermally activated delayed fluorescence organic light emitters. *Angew Chemie Int Ed* **55**, 5739–5744.
31. Liang Q, Xu J, Xue J, Qiao J (2020) Near-infrared-II thermally activated delayed fluorescence organic light-emitting diodes. *Chem Commun* **56**, 8988–8991.
32. Chen H-C, Hsu C-P, Reek JNH, Williams RM, Brouwer AM (2015) Highly soluble benzo[ghi]perylenetriimide derivatives: Stable and air-insensitive electron acceptors for artificial photosynthesis. *ChemSusChem* **8**, 3639–3650.
33. Duan W, Huang J, Kowalski JA, Shkrob IA, Vijayakumar M, Walter E, Pan B, Yang Z, et al (2017) "Wine-Dark Sea" in an organic flow battery: Storing negative charge in 2,1,3-benzothiadiazole radicals leads to improved cyclability. *ACS Energy Lett* **2**, 1156–1161.
34. Paramasivam M, Gupta A, Raynor AM, Bhosale SV, Bhanuprakash K, Jayathirtha Rao V (2014) Small band gap D-$\pi$-A-$\pi$-D benzothiadiazole derivatives with low-lying HOMO levels as potential donors for applications in organic photovoltaics: a combined experimental and theoretical investigation. *RSC Adv* **4**, 35318–35331.
35. Butkute R, Masiulyte A, Rashid EU, Sargsyan S, Moudgalya NS, Leitonas K, Volyniuk D, Grazulevicius JV (2024) Ultralow dark current density of organic photodetectors and organic light-emitting diodes endowed by highly thermally stable derivatives of 2,7-di-tert-butyl-9,9-dimethyl-9,10-dihydroacridine and phenanthroimidazole exhibiting balanced bipolar charge tran. *ACS Appl Electron Mater* **6**, 4735–4745.
36. Han M, Chen Y, Xie Y, Zhang F, Li X, Huang A, Fan Y, Fan Y, et al (2020) 1.42-Fold enhancement of blue OLED device performance by simply changing alkyl groups on the acridine ring. *Cell Rep Phys Sci* **1**, 100252.
37. Yu H, Dai X, Yao F, Wei X, Cao J, Jhun C (2018) Efficient white phosphorescent organic light-emitting diodes using ultrathin emissive layers (<1 nm). *Sci Rep* **8**, 6068.
38. Kim HU, Kim T, Kim C, Kim M, Park T (2023) Recent advances in structural design of efficient near-infrared light-emitting organic small molecules. *Adv Funct Mater* **33**, 2208082.

## Appendix A. Supplementary data

FDMACBz

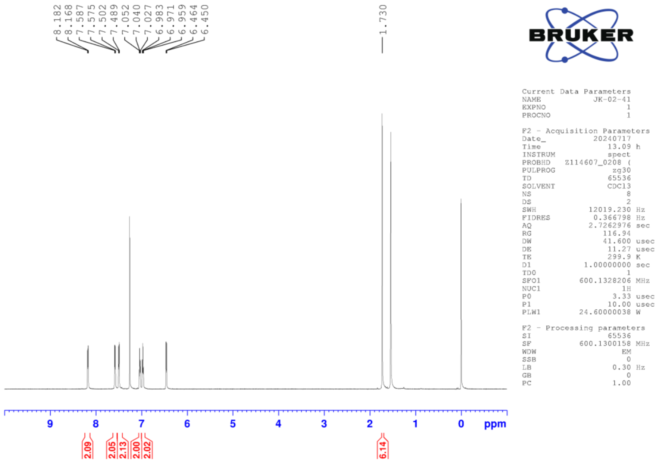

```
Current Data Parameters
NAME              JK-02-41
EXPNO                    1
PROCNO                   1

F2 - Acquisition Parameters
Date_             20240717
Time                 13.09 h
INSTRUM              spect
PROBHD   Z114607_0208 (
PULPROG               zg30
TD                   65536
SOLVENT              CDCl3
NS                       8
DS                       2
SWH              12019.230 Hz
FIDRES            0.366798 Hz
AQ               2.7262976 sec
RG                  116.94
DW                  41.600 usec
DE                   11.27 usec
TE                   299.9 K
D1              1.00000000 sec
TD0                      1
SFO1           600.1328206 MHz
NUC1                    1H
P0                    3.33 usec
P1                   10.00 usec
PLW1           24.60000038 W

F2 - Processing parameters
SI                   65536
SF             600.1300158 MHz
WDW                     EM
SSB                      0
LB                    0.30 Hz
GB                       0
PC                    1.00
```

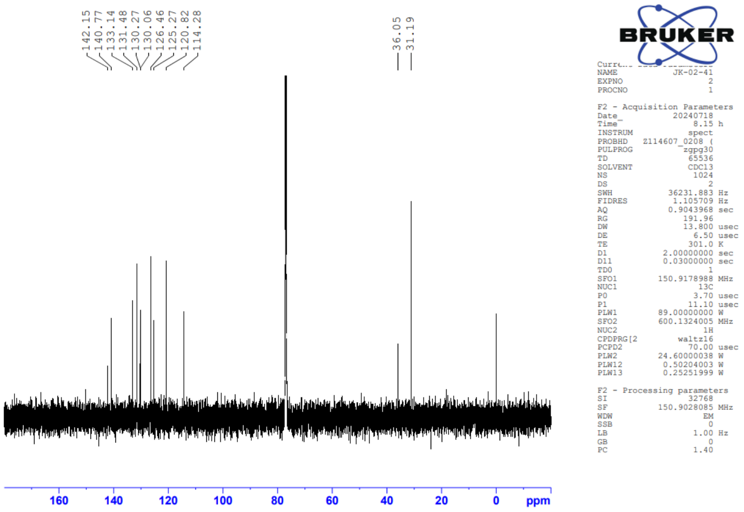

```
Curr...
NAME              JK-02-41
EXPNO                    2
PROCNO                   1

F2 - Acquisition Parameters
Date_             20240718
Time                  8.15 h
INSTRUM              spect
PROBHD   Z114607_0208 (
PULPROG             zgpg30
TD                   65536
SOLVENT              CDCl3
NS                    1024
DS                       2
SWH              36231.883 Hz
FIDRES            1.105709 Hz
AQ               0.9043968 sec
RG                  191.96
DW                  13.800 usec
DE                    6.50 usec
TE                   301.0 K
D1              2.00000000 sec
D11             0.03000000 sec
TD0                      1
SFO1           150.9178988 MHz
NUC1                   13C
P0                    3.70 usec
P1                   11.10 usec
PLW1           89.00000000 W
SFO2           600.1324005 MHz
NUC2                    1H
CPDPRG[2           waltz16
PCPD2                70.00 usec
PLW2           24.60000038 W
PLW12           0.50204003 W
PLW13           0.25251999 W

F2 - Processing parameters
SI                   32768
SF             150.9028085 MHz
WDW                     EM
SSB                      0
LB                    1.00 Hz
GB                       0
PC                    1.40
```

**MALDI-TOF-MS Report**

**Frontier Research Center, Vidyasirimedhi Institute of Science and Technology**

*Comment 1*
*Comment 2*

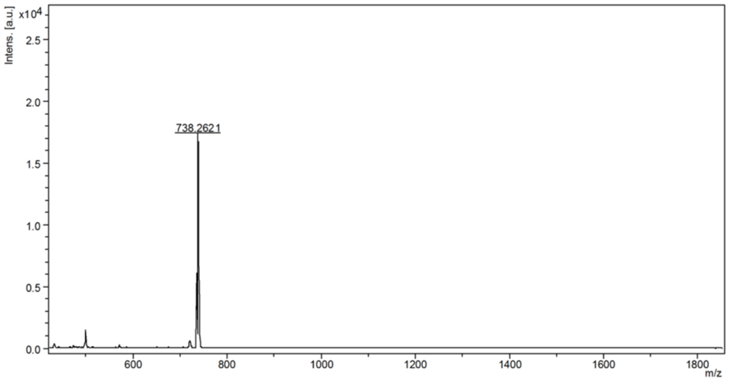

**Fig. S1** Copies of NMR spectra and HRMS mass.

DMACCNBz

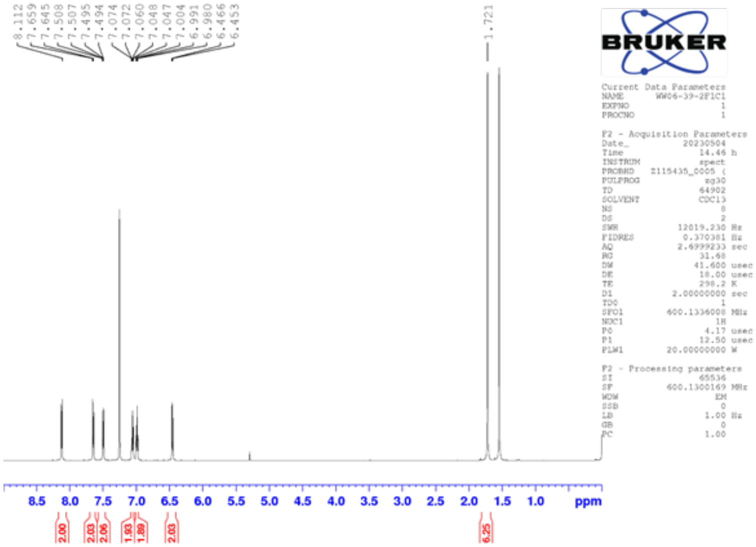

```
Current Data Parameters
NAME        WW06-39-2F1C1
EXPNO                   1
PROCNO                  1

F2 - Acquisition Parameters
Date_            20230504
Time                14.46 h
INSTRUM             spect
PROBHD   Z115435_0005 (
PULPROG              zg30
TD                  64902
SOLVENT             CDCl3
NS                      8
DS                      2
SWH             12019.230 Hz
FIDRES           0.370381 Hz
AQ              2.6999233 sec
RG                  31.68
DW                 41.600 usec
DE                  18.00 usec
TE                  298.2 K
D1             2.00000000 sec
TD0                     1
SFO1          600.1336008 MHz
NUC1                   1H
P0                   4.17 usec
P1                  12.50 usec
PLW1          20.00000000 W

F2 - Processing parameters
SI                  65536
SF            600.1300169 MHz
WDW                    EM
SSB                     0
LB                   1.00 Hz
GB                      0
PC                   1.00
```

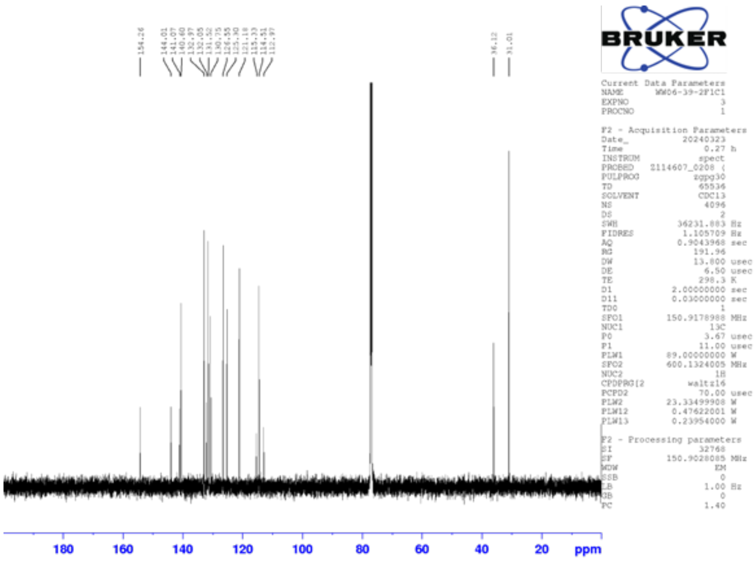

```
Current Data Parameters
NAME        WW06-39-2F1C1
EXPNO                   3
PROCNO                  1

F2 - Acquisition Parameters
Date_            20240323
Time                 0.27 h
INSTRUM             spect
PROBHD   Z114607_0208 (
PULPROG            zgpg30
TD                  65536
SOLVENT             CDCl3
NS                   4096
DS                      2
SWH             36231.883 Hz
FIDRES           1.105709 Hz
AQ              0.9043968 sec
RG                 191.96
DW                 13.800 usec
DE                   6.50 usec
TE                  298.3 K
D1             2.00000000 sec
D11            0.03000000 sec
TD0                     1
SFO1          150.9178988 MHz
NUC1                  13C
P0                   3.67 usec
P1                  11.00 usec
PLW1          89.00000000 W
SFO2          600.1324005 MHz
NUC2                   1H
CPDPRG[2           waltz16
PCPD2               70.00 usec
PLW2          23.33499908 W
PLW12          0.47622001 W
PLW13          0.23954000 W

F2 - Processing parameters
SI                  32768
SF            150.9028085 MHz
WDW                    EM
SSB                     0
LB                   1.00 Hz
GB                      0
PC                   1.40
```

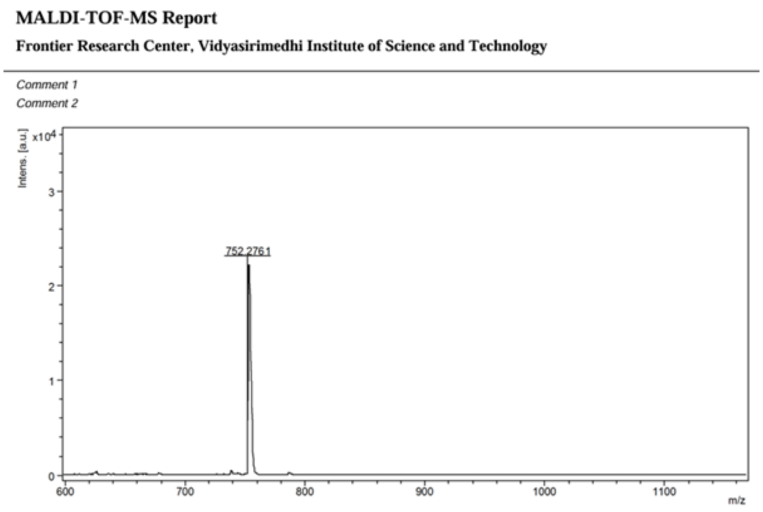

**MALDI-TOF-MS Report**

**Frontier Research Center, Vidyasirimedhi Institute of Science and Technology**

*Comment 1*

*Comment 2*

**Fig. S1** Continue . . . .

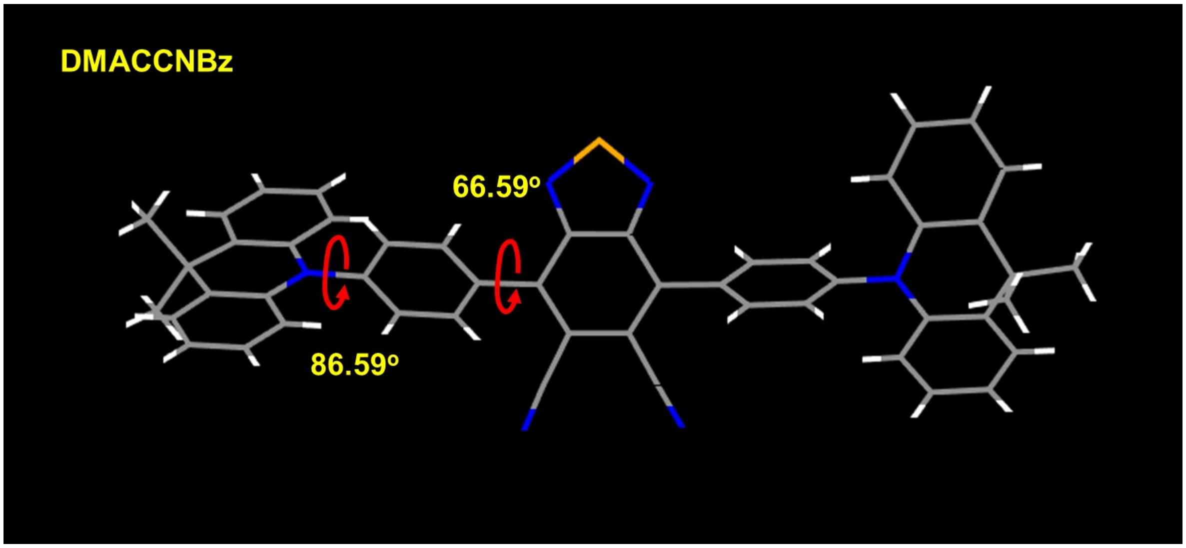

**Fig. S2** Crystal structure of DMACCNBz with 50% probability at 100 K. Label: C = grey, N = blue, S = yellow, and H = white.

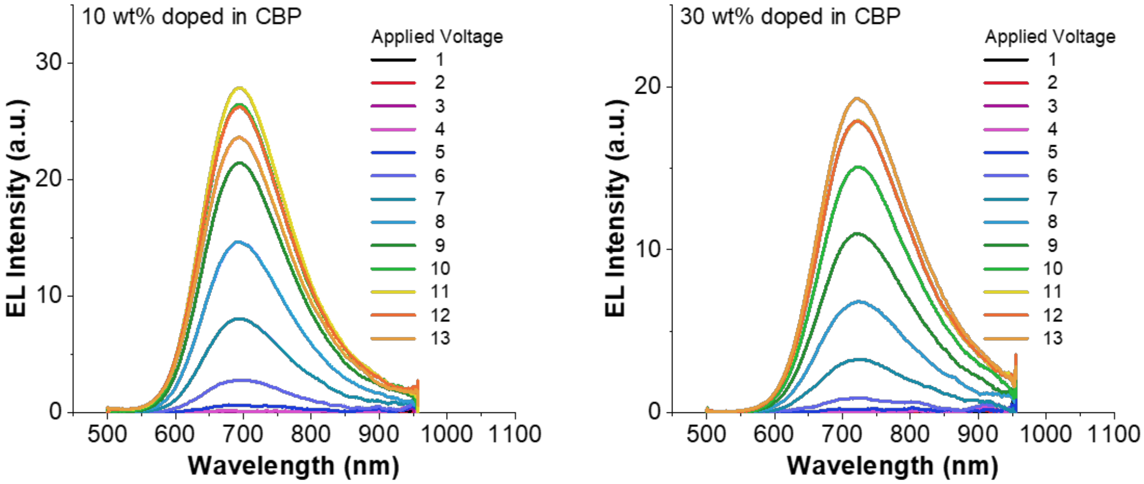

**Fig. S3** EL spectra of the fabricated OLED at different applied voltages.

**Table S1** Crystallographic data table of DMACCNBz.

| Compound | DMACCNBz |
|---|---|
| CCDC deposit number | 2371981 |
| Empirical formula | $C_{50}H_{36}N_6S$ |
| Formula weight | 752.91 |
| Temperature/K | 100 |
| Crystal system | monoclinic |
| Space group | $P2_{1/n}$ |
| $a$/Å<br>$b$/Å<br>$c$/Å | 7.0601(6)<br>13.1064(11)<br>42.680(3) |
| $\alpha/°$<br>$\beta/°$<br>$\gamma/°$ | 90<br>94.5<br>90 |
| Volume/$Å^3$ | 3936.6(5) |
| Z | 4 |
| $\rho_{calc}$ ($g/cm^3$) | 1.270 |
| $\mu/mm^{-1}$ | 0.127 |
| F(000) | 1576.0 |
| Crystal size/$mm^3$ | 0.4 × 0.2 × 0.2 |
| Radiation | MoK$\alpha$ ($\lambda = 0.71073$) |
| 2Θ range for data collection/° | 3.83 to 52.798 |
| Index ranges | $-8 \leqslant h \leqslant 8$, $-16 \leqslant k \leqslant 16$, $-53 \leqslant l \leqslant 53$ |
| Reflections collected | 163439 |
| Independent reflections | 8052 [$R_{int} = 0.0528$, $R_{sigma} = 0.0179$] |
| Data/restraints/parameters | 8052/0/519 |
| Goodness-of-fit on $F^2$ | 1.095 |
| Final R indexes [$I \geqslant 2\sigma$ (I)] | $R_1 = 0.0369$, $wR_2 = 0.0878$ |
| Final R indexes [all data] | $R_1 = 0.0443$, $wR_2 = 0.0969$ |